SUPPLEMENTARY INFORMATION

Direct Observation of the Local Reaction Environment during the Electrochemical Reduction of CO_2

Ezra L. Clark[1,2] and Alexis T. Bell*[1,2]

[1]Joint Center for Artificial Photosynthesis
Lawrence Berkeley National Laboratory
Berkeley, CA 94720
[2]Department of Chemical and Biomolecular Engineering
University of California
Berkeley, CA 94720

Submitted to
Journal of the American Chemical Society

* To whom correspondence should be sent: alexbell@berkeley.edu

SUPPLEMENTARY INFORMATION

Table of Contents

SI-1: Optimization of the Metallic Thin Film Thickness S-03

SI-2: Validating Surface Purity by X-Ray Photoelectron and Ion-Scattering Spectroscopies S-05

SI-3: Quantifying the Uncompensated Resistance of the DEMS Cell S-06

SI-4: Quantifying the Relative Electrochemical Surface Area of the DEMS Electrode S-07

SI-5: Mass Spectra of Reactants and Products S-08

SI-6: H_2 Calibration Procedure S-10

SI-7: H_2 Evolution Linear Sweep Voltammetry over Ag vs Scan Rate S-12

SI-8: Calculated Signal Contributions over Ag S-13

SI-9: CO Calibration Procedure S-14

SI-10: Linear Sweep Voltammetry over Ag vs Scan Rate S-15

SI-11: CO_2 Signal vs Flow Rate S-17

SI-12: Linear Sweep Voltammetry over Ag vs Electrolyte Flow Rate S-18

SI-13: Chronoamperometry Staircase over Ag vs CO_2 Flow Rate in an H-Cell S-20

SI-14: Calculated Signal Contributions over Cu S-21

SI-15: Deconvolution of the Mass-Ion Currents Observed over Cu S-22

SI-16: Transient Ethene Generation Rate Before and After Cathodic Polarization S-24

SI-17: Analysis of the Pervaporate Collected over Cu by Liquid Chromatography S-25

SI-1: Optimization of the Metallic Thin Film Thickness

Ag thin films were deposited onto the nanoporous PTFE membrane to effective thicknesses of 100 to 600 nm. X-ray diffractograms of each Ag thin film were measured, as shown in Figure S1A. The diffractograms were utilized to calculate the average crystallite size using the Scherrer equation, as shown in Figure S1B. Scanning electron micrographs were recorded for each thin film, as shown in Figure S2. Ag thin films with low effective thicknesses result in minimal coating of the PTFE fibers, which could compromise the electrical continuity of the electrocatalyst layer. Conversely, Ag thin films with high effective thicknesses begin to block the nanopores in the PTFE membrane, which will compromise the efficiency of product collection. Thus, the optimal film thickness was determined by measuring the slope of the H_2 calibration curve and the maximum CO signal (m/z = 28) during linear sweep voltammetry. As shown in Figure S3A, Ag thin films with effective thicknesses greater than 400 nm resulted in a reduced sensitivity to H_2, presumably due to a reduced collection efficiency resulting from the blocking of the nanopores in the PTFE membrane. As shown in Figure S3B, the CO signal was maximized

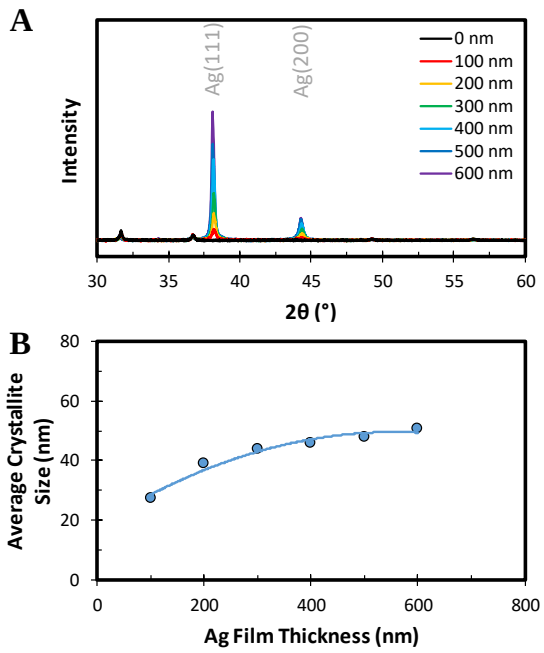

Figure S1 – (A) X-ray diffractograms of the Ag thin film on the nanoporous PTFE membrane as a function of the effective thickness. (B) Average crystallite size of the Ag thin films deposited on the nanoporous PTFE membrane, as calculated using the Scherrer equation.

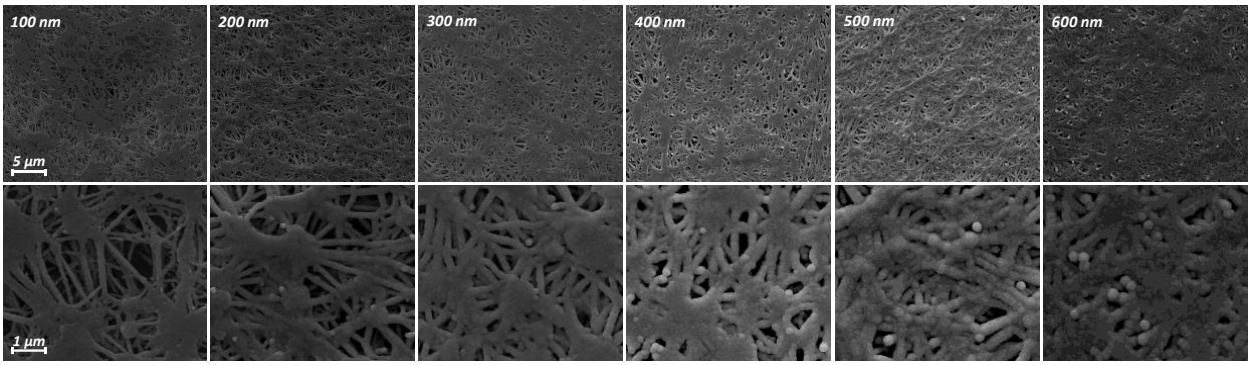

Figure S2 – Scanning electron micrographs of the Ag thin films deposited onto the nanoporous PTFE membrane to different effective thicknesses.

over Ag thin films with an effective thickness of 400 nm. The CO signal at lower and higher thicknesses decreases presumable due to the excessive depletion of CO_2 due to pervaporation and the reduced product collection efficiency, respectively.

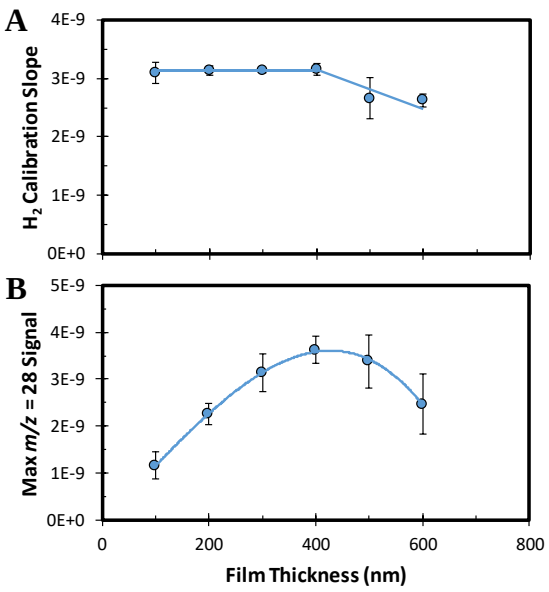

Figure S3 – Impact of Ag film thickness on: (A) H_2 calibration curve slope and (B) maximum CO signal (m/z = 28) observed during linear sweep voltammetry.

SI-2: Validating Surface Purity by X-Ray Photoelectron and Ion-Scattering Spectroscopies

The purity of the working electrode surface was validated before and after experimentation using x-ray photoelectron (XPS) and ion scattering spectroscopies (ISS). As shown in Figure S4, no impurities were detected before or after experimentation by either analytical technique over a representative Ag thin film deposited onto the nanoporous PTFE membrane.

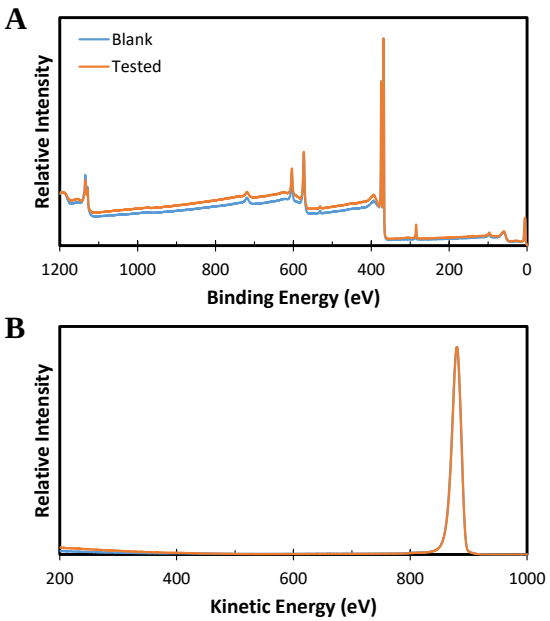

Figure S4 – Analysis of a representative Ag thin film deposited on the nanoporous PTFE membrane before and after experimentation by: (A) XPS and (B) ISS.

SI-3: Quantifying the Uncompensated Resistance of the DEMS Cell

The uncompensated resistance of the electrochemical cell was determined by potentiostatic electrochemical impedance spectroscopy. The uncompensated resistance was found to be ~60 Ω at electrolyte flow rates of 0 to 85 mL/min when the voltage waveforms were centered at the open circuit potential, as shown in Figure S5A. Furthermore, the uncompensated resistance was found to be ~60 Ω when the voltage waveforms were centered at increasingly cathodic potentials using an electrolyte flow rate of 85 mL/min, as shown in Figure S5B.

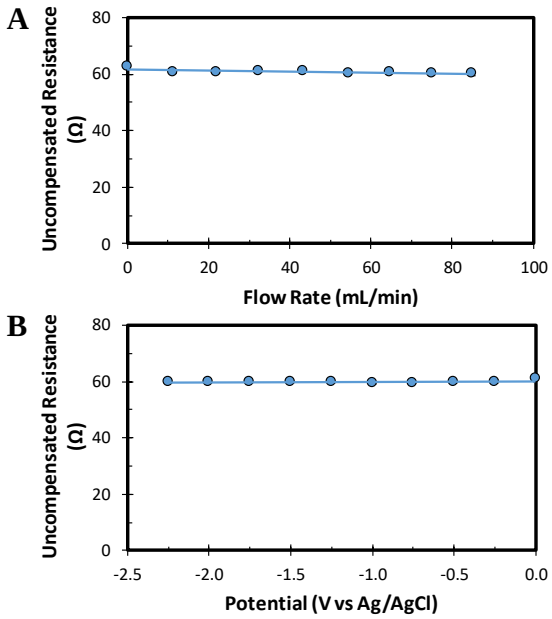

Figure S5 – Uncompensated resistance of the electrochemical cell as determined using potentiostatic electrochemical impedance spectroscopy: (A) as a function of flow rate with voltage waveforms centered at the open circuit potential and (B) with voltage waveforms centered at increasingly cathodic potentials at a flow rate of 85 mL/min.

The uncompensated resistance of the electrochemical cell was also determined using the current interrupt technique. The uncompensated resistance was found to be ~65 Ω at electrolyte flow rates of 0 to 85 mL/min when the interrupted current density was 40 mA/cm^2, as shown in Figure S6A. Furthermore, the uncompensated resistance was also found to be ~65 Ω when the interrupted current density was increasingly cathodic using an electrolyte flow rate of 85 mL/min, as shown in Figure S6B.

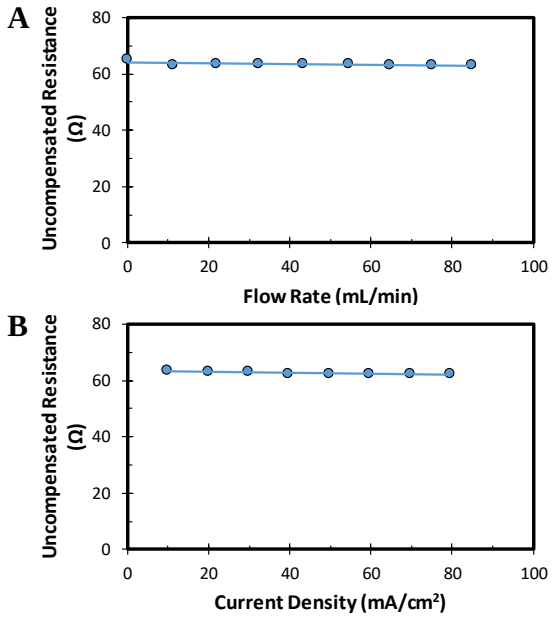

Figure 6 – Uncompensated resistance of the electrochemical cell as determined using the current interrupt technique: (A) as a function of flow rate using an interrupted current density of 20 mA/cm^2 and (B) with an increasingly cathodic interrupted current density at a flow rate of 85 mL/min.

SI-4: Quantifying the Relative Electrochemical Surface Area of the DEMS Electrode

The roughness factor of the DEMS electrode was compared to an analogous thin film deposited on a polished Si wafer by taking the ratio of their double layer capacitances. The double layer capacitance of each electrode was determined by measuring the charging current in a potential range where no Faradaic processes occur at a series of increasingly rapid scan rates, as shown in Figure S7A. As shown in Figure S7B, the DEMS electrode had a roughness factor of ~2.9 relative to the thin film deposited on a polished Si wafer.

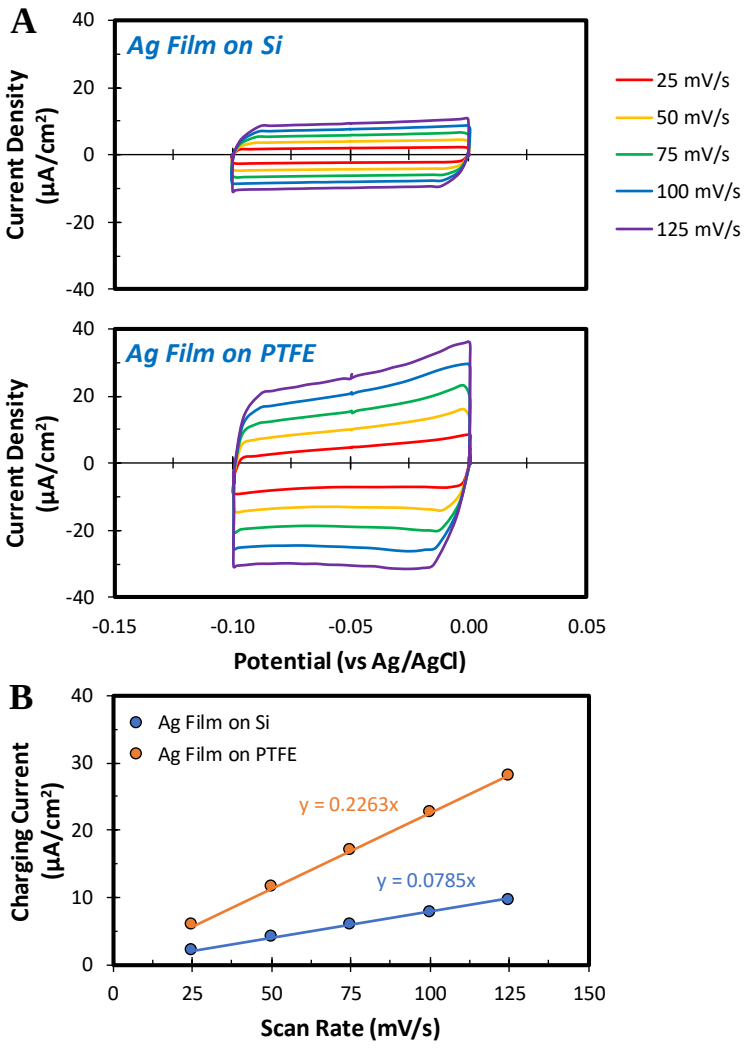

Figure S7 – (A) Cyclic voltammetry in a potential range where no Faradaic processes occur at a series of increasingly rapid scan rates over Ag thin films deposited onto a polished Si wafer and the nanoporous PTFE membrane. (B) Comparison of the double layer capacitances of the Ag thin films deposited onto a polished Si wafer and the nanoporous PTFE membrane.

SI-5: Mass Spectra of Reactants and Products

The mass spectra of CO_2, CO, and ethene were measured by feeding a standard gas into the mass spectrometer to enable accurate deconvolution of the *m/z* = 28 mass-ion current, as shown in Figure S8. The mass spectra of acetaldehyde, ethanol, allyl alcohol, propionaldehyde, and n-propanol were measured by analyzing 50 mM solutions of each species to enable accurate deconvolution of the *m/z* = 31, 43, 57, 58, and 59 mass-ion currents, as shown in Figure S9.

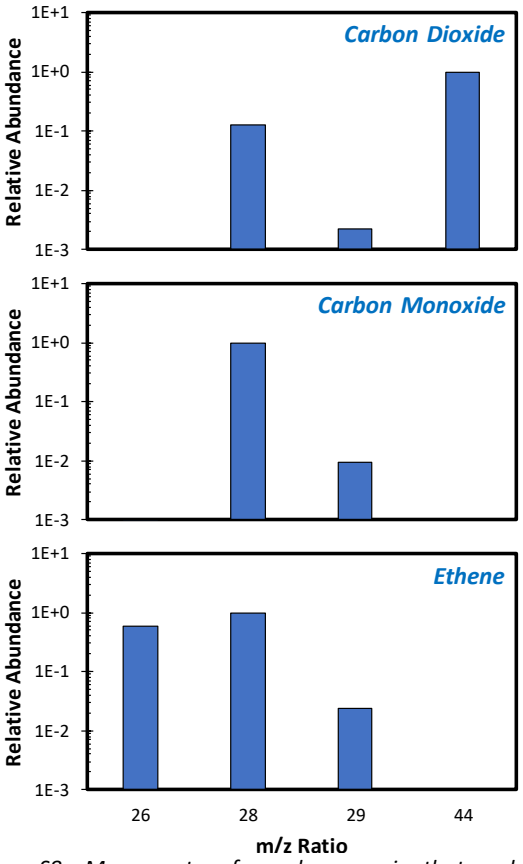

Figure S8 – Mass spectra of gas phase species that produce the m/z = 28 fragment upon ionization.

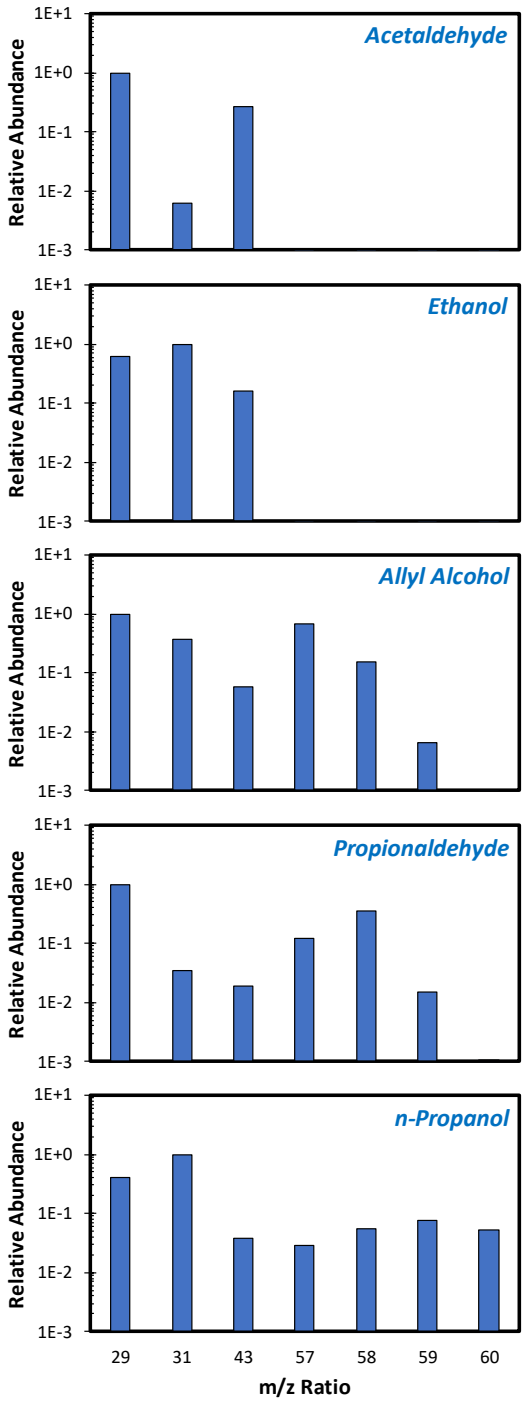

Figure S9 – Mass spectra of the primary liquid phase products produced over Cu as measured by analyzing 50 mM standard solutions of each product.

SI-6: H_2 Calibration Procedure

The signal response of the mass spectrometer to the evolution of H_2 was calibrated by conducting a chronopotentiometry staircase from 2 to 40 mA/cm^2 with a step length of 10 s while monitoring the *m/z* = 2 mass-ion current, as shown in Figure S10A. As shown in Figure S10B, a linear correlation between the *m/z* = 2 mass-ion current signal and the total current density was observed. The chronopotentiometry staircase was repeated several times to demonstrate the reproducibility of the H_2 calibration curve, which indicates that the product collection efficiency does not vary with extended operation, as shown in Figure S11. Finally, the chronopotentiometry staircase was conducted at increasingly rapid electrolyte flow rates to determine the impact that electrolyte convection has on the efficiency of product collection. The collection efficiency was assumed to be 100% under stagnant electrolyte conditions. As shown in Figure S12, the collection efficiency was found to decrease linearly with flow rate but was still greater than 80% at the maximum flow rate employed in the study.

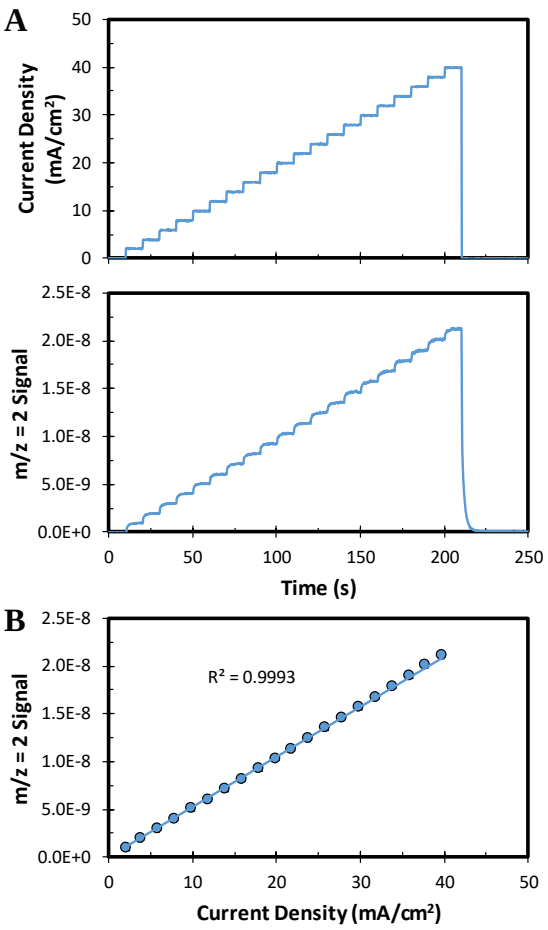

Figure S10 – H_2 calibration protocol: (A) chronopotentiometry staircase. (B) H_2 calibration curve.

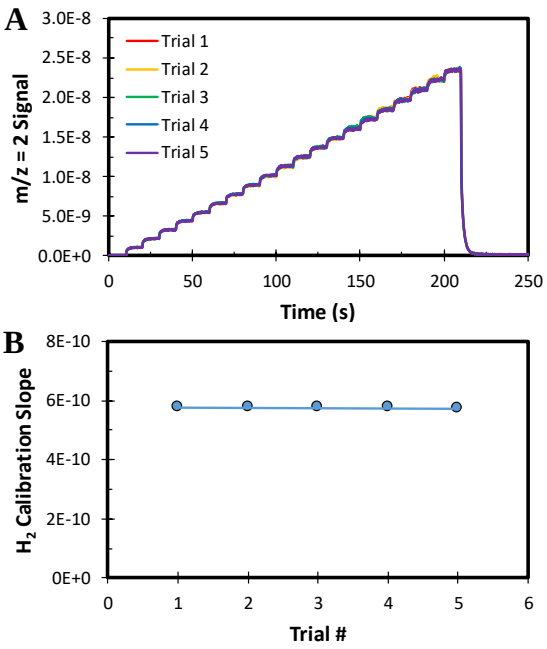

Figure S11 – (A) m/z = 2 signal observed during 5 successive chronopotentiometry staircases. (B) Slope of H_2 calibration curve as a function of the trial number.

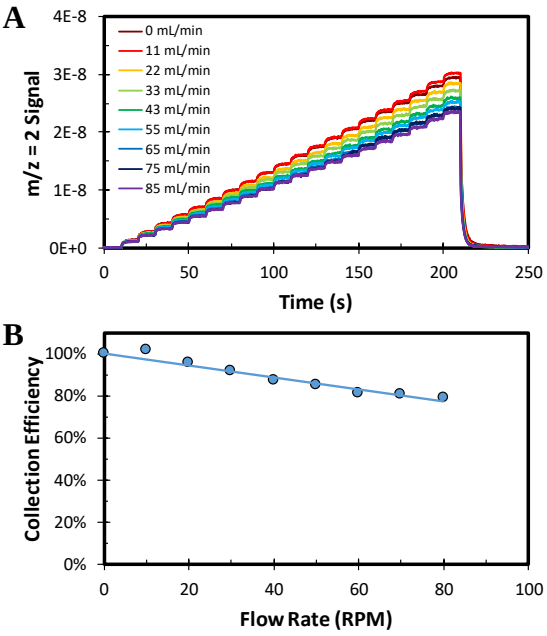

Figure 12 – (A) m/z = 2 signal observed during chronopotentiometry staircases at increasingly rapid electrolyte flow rates. (B) H_2 collection efficiency vs flow rate calculated assuming complete collection under stagnant conditions.

SI-7: H_2 Evolution Linear Sweep Voltammetry over Ag vs Scan Rate

The total fraction of H_2 generated during linear sweep voltammetry that was detected by mass spectrometry is shown in Figure S13. It is apparent that the total amount of H_2 generated during the scan that is detected by mass spectrometry begins to decline slightly at scan rates faster than 50 mV/s. However, a greater fraction of this H_2 is detected after the scan ends due to the finite time associated with mass transfer from the electrode surface into the mass spectrometer. This issue was compounded by the fact that products generated at the electrode surface can either pervaporate into the mass spectrometer or diffuse into the bulk of the electrolyte, as shown in Figure S14. Once the scan ends and the product concentration near the electrode surface is rapidly diminished by pervaporation, causing products that diffused away from the electrode surface to diffuse back and pervaporate, causing an exponential decline in the mass-ion current signals after Faradaic charge transfer ceases. This phenomenon was only significant for H_2 because it diffuses much more rapidly into the electrolyte than other reaction products.

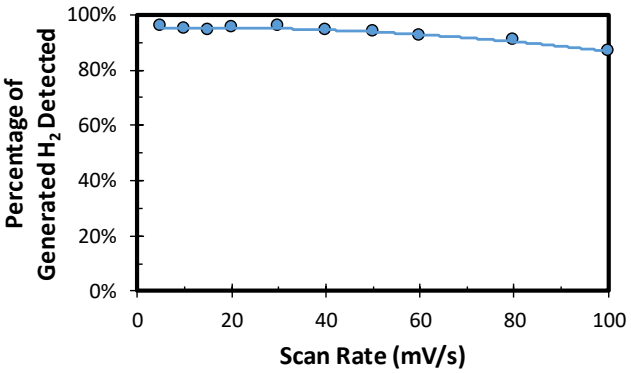

Figure S13 – Total percentage of generated H_2 that is detected by mass spectrometry during linear sweep voltammetry as a function of the scan rate.

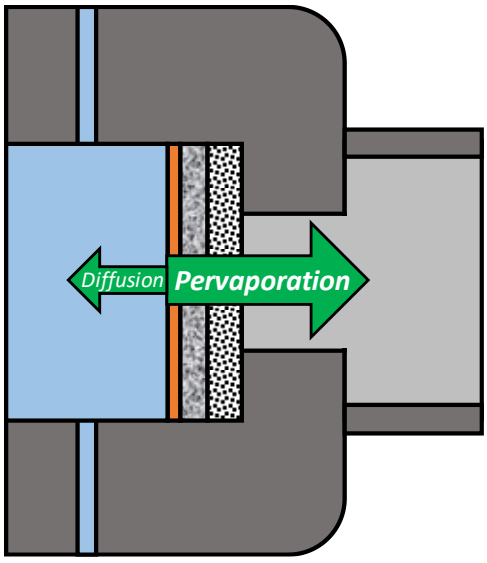

Figure S14 – Directions of product flux at the surface of the DEMS electrode. Arrow sizes indicate relative magnitudes.

SI-8: Calculated Signal Contributions over Ag

The contributions of different species to the expected mass spectrum over Ag at an applied potential of -1 V vs RHE were calculated to determine which mass-ion currents should be monitored using:

$$Contribution\ of\ species\ i\ to\ {}^{m}/_{z} = j\ Signal = \frac{\dot{n}_i \frac{Im_{/z=j,i}}{\sum_j Im_{/z=j,i}}}{\sum_i \dot{n}_i \frac{Im_{/z=j,i}}{\sum_j Im_{/z=j,i}}} \quad (1)$$

Where:

$\dot{n}_i$ Flux of species i at the electrode surface (nmol/min)

$Im_{/z=j,i}$ Relative intensity of *m/z* = j for species i

The results of this calculation are shown in Table S1. There is no mass-ion current that is solely produced by the ionization of CO, necessitating the contributions of CO_2 to the observed mass spectrum to be deconvoluted to obtain a mass-ion current signal that is directly proportional to the generation rate of CO.

Table S1 – Calculated contributions of reactants and products to the expected mass spectrum over Ag at -1 V vs RHE.

m/z Ratio	Primary Contributor	Calculated Contribution	Other Contributors
2	H_2	100.00%	N/A
28	CO	91.34%	CO_2 (8.66%)
44	CO_2	100.00%	N/A

SI-9: CO Calibration Procedure

CO calibration was conducted in an analogous way as H_2 calibration, except that the mass-ion currents for *m/z* = 2, 28, and 44 were all monitored during the chronopotentiometry staircase, as shown in Figure S15. Furthermore, the chonopotentiometry staircase was conducted from high current density to low current density during CO calibration. This was done because the rate of CO evolution exhibited transient changes at low current density, which compromised accurate quantification. However, if high current densities were applied before the application of low current densities then the CO partial current density did not exhibit transient changes at low current density. Thus, CO calibration was accomplish using chronopotentiometry staircases from high current density to low current density to improve the accuracy of CO quantification. The CO partial current density was assumed to be equivalent to the difference between the total current density and the H_2 partial current density, which was determined using the observed *m/z* = 2 mass-ion current and the H_2 calibration curve. The contribution of CO_2 to the observed *m/z* = 28 signal was accounted for using the observed *m/z* = 44 mass-ion current and the measured mass spectrum of CO_2. The results of this analysis are shown in Figure S16A. A linear correlation between the deconvoluted *m/z* = 28 mass-ion current signal and the calculated CO partial current density was obtained, as shown in Figure S16B.

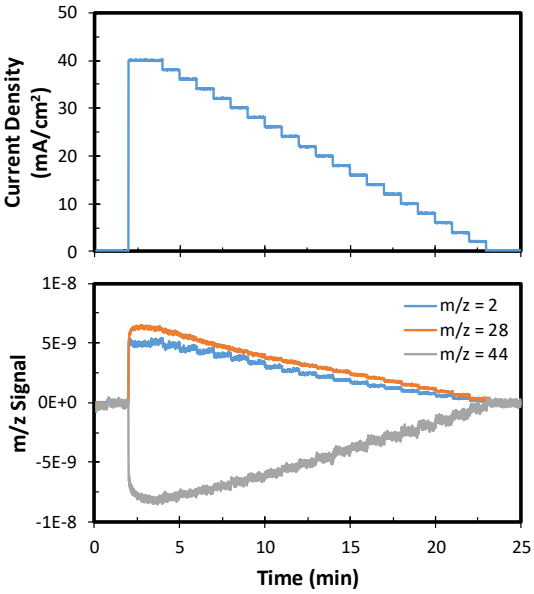

Figure S15 – CO calibration chronopotentiometry staircase.

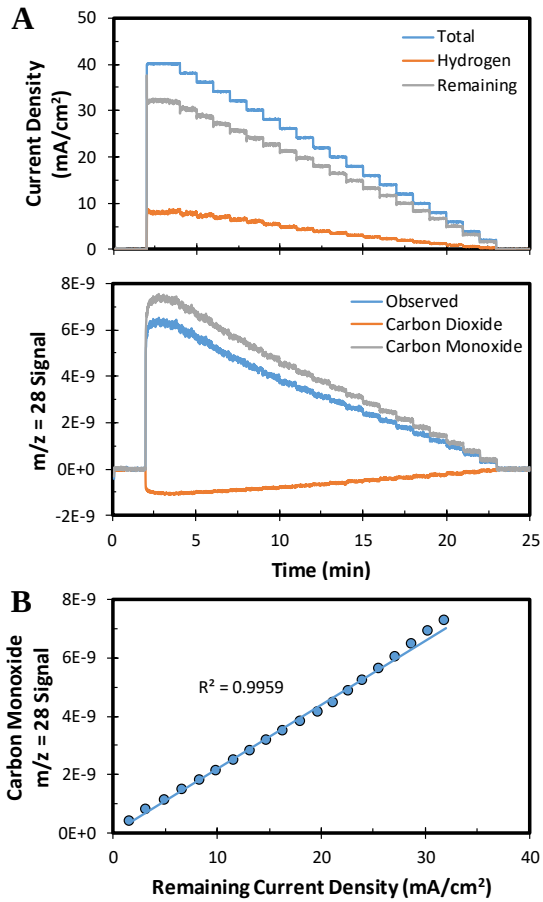

Figure S16 – (A) Calculation of the CO partial current density and m/z = 28 signal due to the ionization of CO during the chronopotentiometry staircase. (B) CO calibration curve.

SI-10: Linear Sweep Voltammetry over Ag vs Scan Rate

Linear sweep voltammetry was conducted over Ag at different scan rates. As shown in Figure S17, the overall current evolved at a given potential was found to be independent of the scan rate employed. However, the H_2 partial current density decreased and the CO partial current density increased at a fixed potential as the scan rate was increased from 5 to 20 mV/s. However, the H_2 and CO partial current densities did not change further when scan rates faster than 20 mV/s were employed. These changes resulted in a reduced H_2 Faradaic efficiency and an enhanced CO Faradaic efficiency at a fixed potential as the scan rate was increased from 5 to 20 mV/s, with no additional changes for scan rates faster than 20 mV/s.

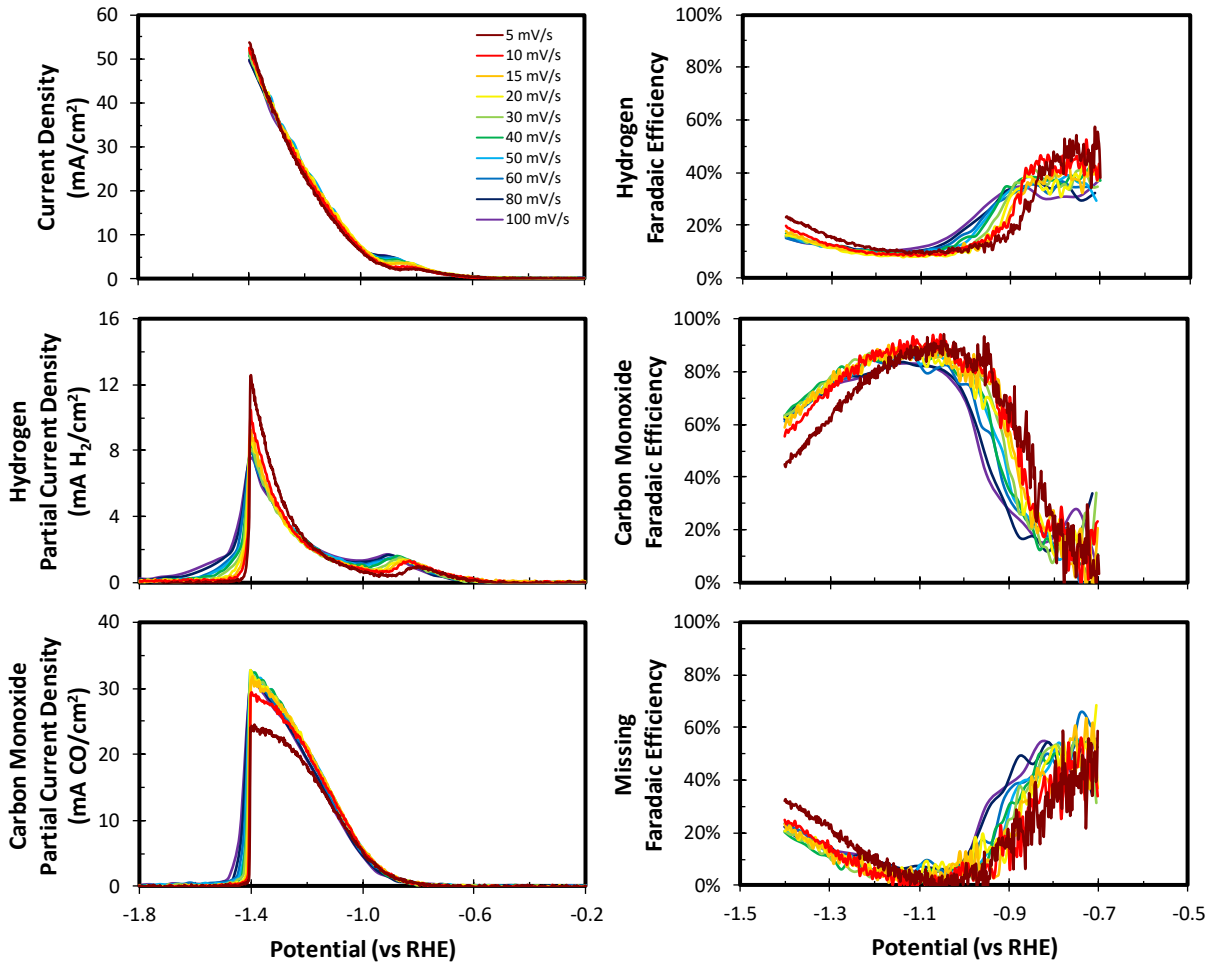

Figure S17 – CO_2 reduction activity of Ag measured during linear sweep voltammetry at a series of increasingly rapid scan rates in 0.1 M $CsHCO_3$ at a flow rate of 85 mL/min.

To understand the origin of these activity trends the scan rate dependence of the local CO_2 concentration was investigated. As shown in Figure S18, the local CO_2 concentration was found to be

independent of the scan rate at a given potential, despite the differences in the rates of CO evolution for scan rates below 20 mV/s. This suggests that there is a second mode of CO_2 depletion that is responsible for depleting a greater fraction of the local CO_2 concentration as the scan rate drops below 20 mV/s.

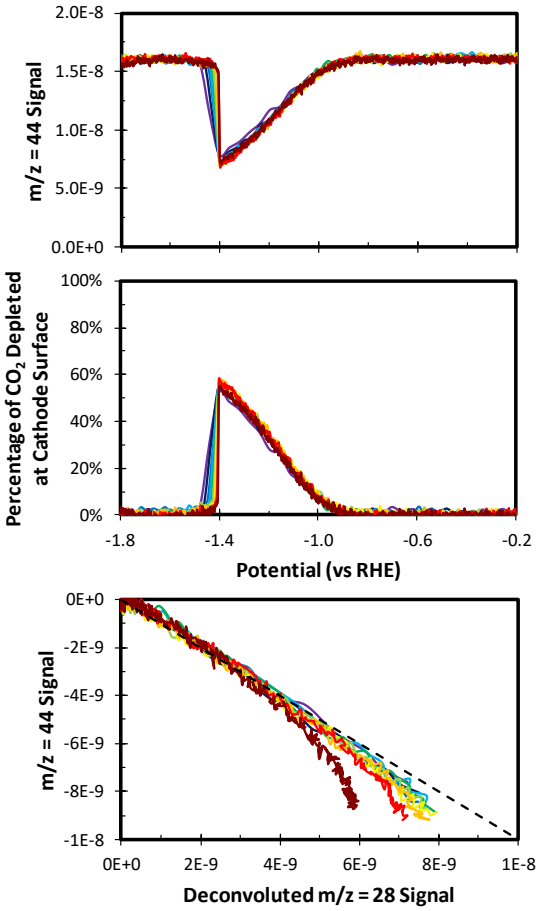

Figure S18 – Local CO_2 concentration observed over Ag during linear sweep voltammetry at a series of increasingly rapid scan rates in 0.1 M $CsHCO_3$ at a flow rate of 85 mL/min.

SI-11: CO_2 Signal vs Flow Rate

The steady state *m/z* = 44 signal was monitored as a function of the electrolyte flow rate to determine the impact that the flow rate has on the flux of CO_2 to the cathode surface. As shown on Figure S19, as the electrolyte flow rate increases the rate of CO_2 supply to the cathode increases, as reflected by the increased *m/z* = 44 mass-ion current signal. This occurs because higher electrolyte flow rates result in a reduced hydrodynamic and mass transfer boundary layer thickness at the cathode surface. However, the flux of CO_2 to the cathode surface begins to plateau at electrolyte flow rates faster than 70 mL/min.

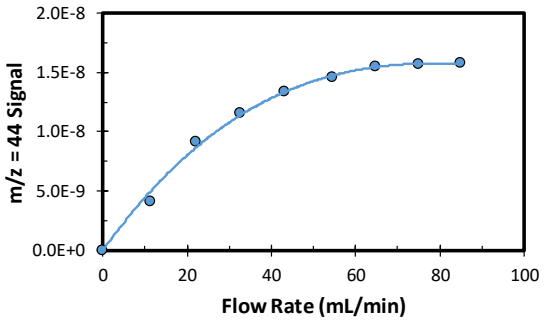

Figure S19 – Dependence of the CO_2 signal (m/z = 44) on the electrolyte flow rate.

SI-12: Linear Sweep Voltammetry over Ag vs Flow Rate

Linear sweep voltammetry was conducted over Ag at a scan rate of 5 mV/s using different electrolyte flow rates. As shown in Figure S20, the overall current evolved at a given potential increased with the electrolyte flow rate. Furthermore, the H_2 partial current density decreased and the CO partial current density increased at a fixed potential as the electrolyte flow rate was increased. These changes resulted in a reduced H_2 Faradaic efficiency and an enhanced CO Faradaic efficiency at a fixed potential as the as the electrolyte flow rate was increased.

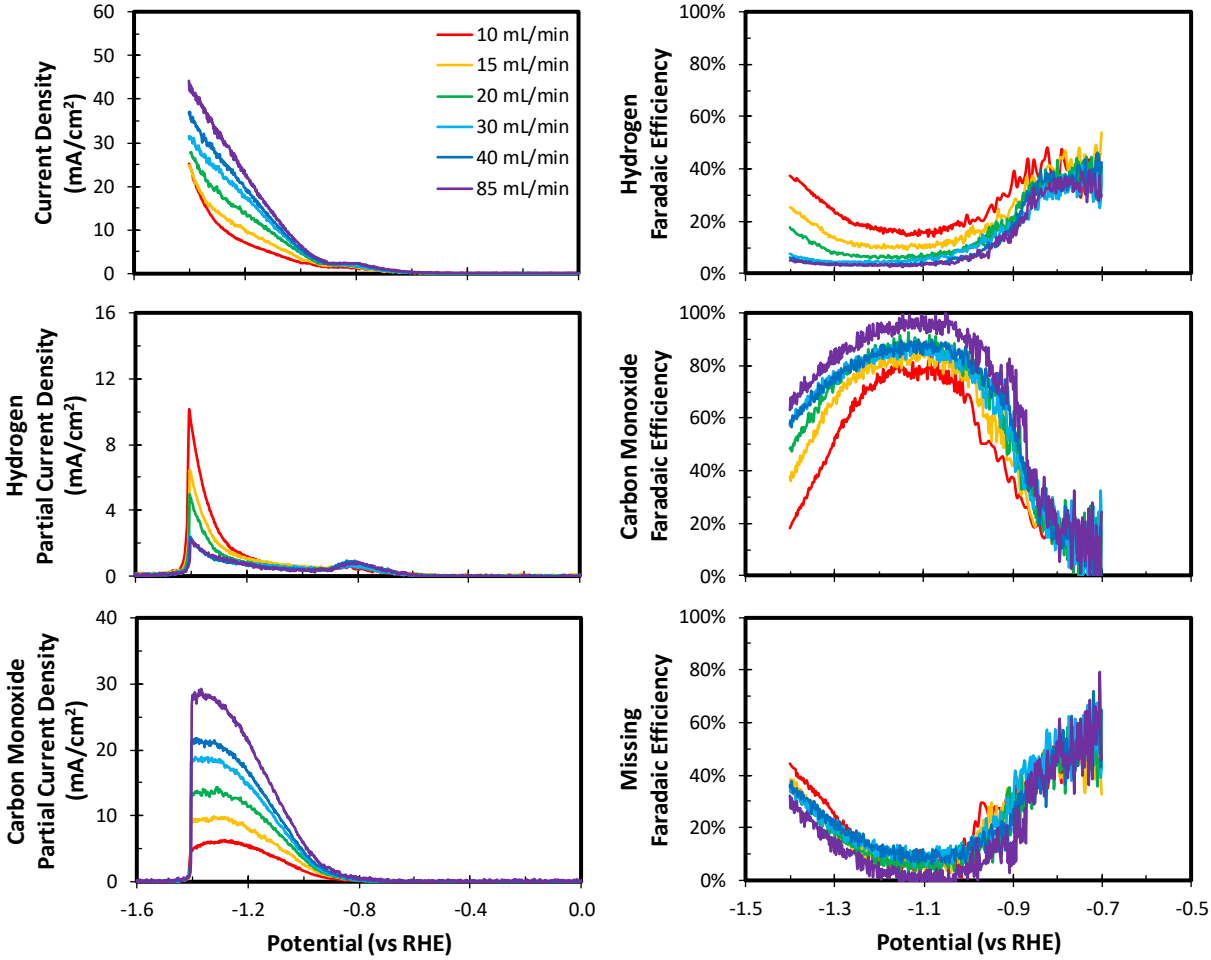

Figure S20 – CO_2 reduction activity of Ag measured during linear sweep voltammetry at a scan rate of 5 mV/s in 0.1 M $CsHCO_3$ using a series of increasingly rapid electrolyte flow rates.

To understand the origin of these activity trends the flow rate dependence of the local CO_2 concentration was investigated. As shown in Figure S21, as the flow rate increases the CO_2 signal increases in the absence of Faradaic current, as explained in section SI-11. At the terminal potential of the linear

potential sweep there is also a higher concentration of CO_2 near the cathode surface, as evidenced by the increased signal with flow rate. While more CO_2 is consumed by the evolution of CO as the electrolyte flow rate increases, the fractional depletion of CO_2 at the cathode surface decreases as the electrolyte flow rate increases. This is a result of an earlier onset of CO_2 depletion by reaction with hydroxyl anions evolved at the cathode surface as the electrolyte flow rate decreases.

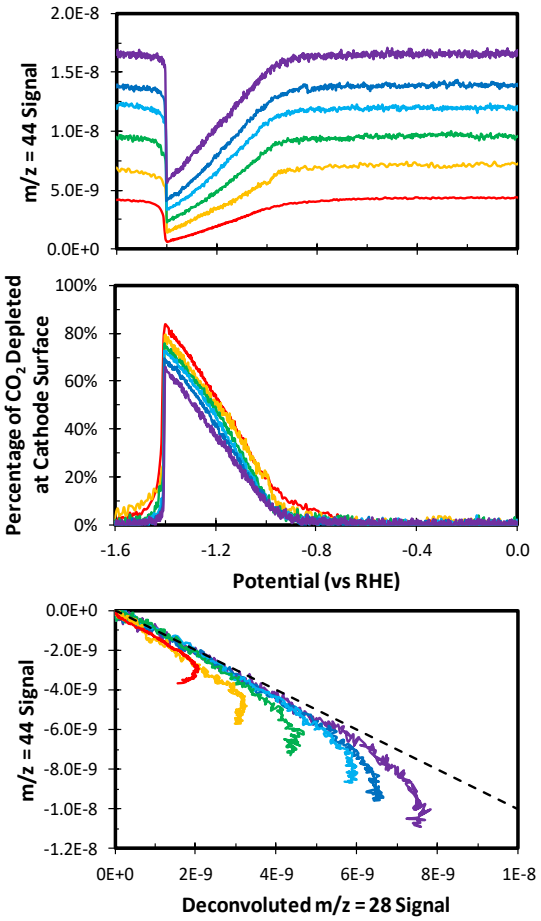

Figure S21 – Local CO_2 concentration observed over Ag during linear sweep voltammetry at a scan rate of 5 mV/s in 0.1 M $CsHCO_3$ using a series of increasingly rapid electrolyte flow rates.

SI-13: Chronoamperometry Staircase over Ag vs CO_2 Flow Rate in an H-Cell

Chronoamperometry staircases were conducted over a polycrystalline Ag film deposited onto a polished Si wafer from -0.5 to -1.5 V vs RHE at increasingly rapid CO_2 flow rates in a traditional H-cell. The electrochemical cell was mixed only by the column of CO_2 bubbles. Thus, as the CO_2 flow rate is increased the hydrodynamic and mass transfer boundary layers at the cathode surface become narrower, improving the rate of CO_2 supply to the cathode. As a result, less H_2 and more CO are generated at a given protentional as the CO_2 flow rate is increased, as shown in Figure S22. This results in a reduced H_2 Faradaic efficiency and an enhanced CO Faradaic efficiency at a fixed potential as the CO_2 flow rate is increased. These trends qualitatively reproduce the trends observed in the DEMS cell at increasingly rapid electrolyte flow rates.

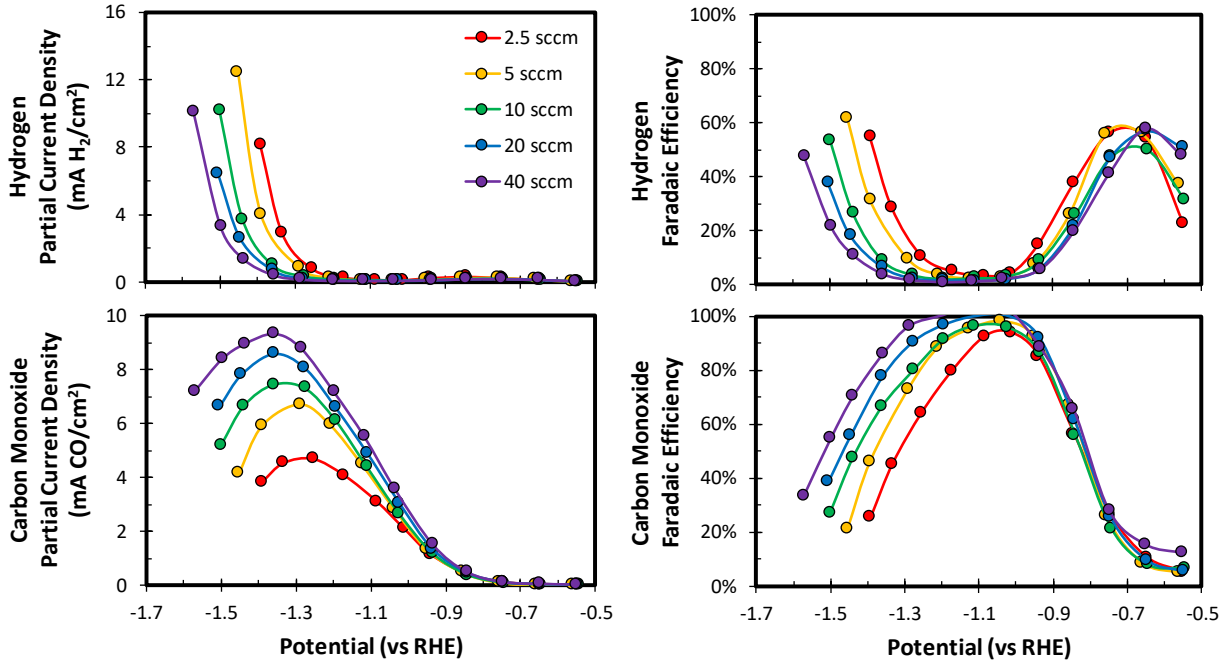

Figure S22 – CO_2 reduction activity of Ag measured during a chronoamperometry staircase in a traditional H-cell in 0.1 M $CsHCO_3$ at a series of increasingly rapid CO_2 flow rates.

SI-14: Calculated Signal Contributions over Cu

The contributions of different species to the expected mass spectrum over Cu at an applied potential of -1.05 V vs RHE were calculated to determine which mass-ion currents should be monitored using:

$$Contribution\ of\ species\ i\ to\ {}^{m}/_{z} = j\ Signal = \frac{\dot{n}_i \frac{I{}^{m}/_{z=j,i}}{\sum_j I{}^{m}/_{z=j,i}}}{\sum_i \dot{n}_i \frac{I{}^{m}/_{z=j,i}}{\sum_j I{}^{m}/_{z=j,i}}} \quad (2)$$

Where:

$\dot{n}_i$ Flux of species i at the electrode surface (nmol/min)

$I{}^{m}/_{z=j,i}$ Relative intensity of m/z = j for species i

The results of this calculation are shown in Table S2. Carbon dioxide (*m/z* = 44), hydrogen (*m/z* = 2), methane (*m/z* = 15), and ethene (*m/z* = 26) are the only species that generate a unique mass fragment upon ionization. The deconvolution strategy for the remaining mass fragments is discussed in SI-15.

Table S2 – Calculated contributions of reactants and products to the expected mass spectrum over Cu at -1.05 V vs RHE.

m/z Ratio	Primary Contributor	Calculated Contribution	Other Contributors
2	H_2	99.21%	Negligible
15	CH_4	98.22%	Negligible
26	C_2H_4	93.12%	CH_3CH_2OH (5.71%)
28	CO_2	48.33%	C_2H_4 (36.05%) CO (15.22%)
31	CH_3CH_2OH	74.67%	$CH_3CH_2CH_2OH$ (23.19%) CH_2CHCH_2OH (1.97%)
43	CH_3CH_2OH	76.18%	CH_3CHO (12.83%) $CH_3CH_2CH_2OH$ (8.93%) CH_2CHCH_2OH (1.86%)
44	CO_2	99.89%	Negligible
57	CH_2CHCH_2OH	80.95%	$CH_3CH_2CH_2OH$ (11.52%) CH_3CH_2CHO (7.53%)
58	CH_3CH_2CHO	62.01%	CH_2CHCH_2OH (37.99%)
59	$CH_3CH_2CH_2OH$	94.88%	CH_3CH_2CHO (3.20%) CH_2CHCH_2OH (1.92%)

SI-15: Deconvolution of the Mass-Ion Currents Observed over Cu

The primary C_3 products produced over Cu are allyl alcohol, propionaldehyde, and n-propanol each of which generate a series of unique mass fragments at *m/z* = 57, 58, and 59 upon ionization. As a result, the extent to which each of these products contributes to the observed mass spectrum can be calculated by solving a system of linear equations:

$$Im_{/z=58,Propion} = \frac{Im_{/z=59} - Im_{/z=58}\frac{Im_{/z=59}}{Im_{/z=58}{}_{n-PrOH}} - (Im_{/z=57} - Im_{/z=58}\frac{Im_{/z=57}}{Im_{/z=58}{}_{n-PrOH}})\frac{(\frac{Im_{/z=59}}{Im_{/z=58}{}_{Allyl}} - \frac{Im_{/z=59}}{Im_{/z=58}{}_{n-PrOH}})}{(\frac{Im_{/z=57}}{Im_{/z=58}{}_{Allyl}} - \frac{Im_{/z=57}}{Im_{/z=58}{}_{n-PrOH}})}}{(\frac{Im_{/z=59}}{Im_{/z=58}{}_{Propion}} - \frac{Im_{/z=59}}{Im_{/z=58}{}_{n-PrOH}}) - (\frac{Im_{/z=57}}{Im_{/z=58}{}_{Propion}} - \frac{Im_{/z=57}}{Im_{/z=58}{}_{n-PrOH}})\frac{(\frac{Im_{/z=59}}{Im_{/z=58}{}_{Propion}} - \frac{Im_{/z=59}}{Im_{/z=58}{}_{n-PrOH}})}{(\frac{Im_{/z=57}}{Im_{/z=58}{}_{Allyl}} - \frac{Im_{/z=57}}{Im_{/z=58}{}_{n-PrOH}})}} \quad (3)$$

$$Im_{/z=58,Allyl} = \frac{Im_{/z=57} - Im_{/z=58}\frac{Im_{/z=57}}{Im_{/z=58}{}_{n-PrOH}} - Im_{/z=58,Propion}(\frac{Im_{/z=57}}{Im_{/z=58}{}_{Propion}} - \frac{Im_{/z=57}}{Im_{/z=58}{}_{n-PrOH}})}{(\frac{Im_{/z=57}}{Im_{/z=58}{}_{Allyl}} - \frac{Im_{/z=57}}{Im_{/z=58}{}_{n-PrOH}})} \quad (4)$$

$$Im_{/z=58,n-PrOH} = Im_{/z=58} - Im_{/z=58,Propion} - Im_{/z=58,Allyl} \quad (5)$$

Where:

$Im_{/z=j}$	Mass-ion current signal for *m/z* = j
$Im_{/z=j,i}$	Mass-ion current signal for *m/z* = j corresponding to product i
$\frac{Im_{/z=j}}{Im_{/z=k}{}_{Product\ i}}$	Intensity of *m/z* = j signal relative to *m/z* = k signal for product i

Once the contributions of the C_3 products to *m/z* = 58 have been analytically calculated their contribution to the other observed mass-ion currents can be calculated using:

$$Im_{/z=j,i} = Im_{/z=k,i}\frac{Im_{/z=j}}{Im_{/z=k}{}_{Product\ i}} \quad (6)$$

Acetaldehyde and ethanol produce a series of mass fragments upon ionization at *m/z* = 31 and 43 that are also unique once the contributions of the C_3 products have been accounted for. Thus, the contributions of acetaldehyde and ethanol to the observed mass spectrum can also be calculated by solving another system of linear equations:

$$Im_{/z=43,Remaining} = Im_{/z=43} - Im_{/z=43,Allyl} - Im_{/z=43,Propion} - Im_{/z=43,n-PrOH} \quad (7)$$

$$Im_{/z=43,Me-CHO} = \frac{Im_{/z=31,Remaining} - Im_{/z=43,Remaining}\frac{Im_{/z=31}}{Im_{/z=43}{}_{EtOH}}}{(\frac{Im_{/z=31}}{Im_{/z=43}{}_{Me-CHO}} - \frac{Im_{/z=31}}{Im_{/z=43}{}_{EtOH}})} \quad (8)$$

$$Im_{/z=43,EtOH} = Im_{/z=43,Remaining} - Im_{/z=43,Me-CHO} \quad (9)$$

The results of this deconvolution protocol are shown in Figure S23, which displays the observed mass-ion currents for m/z = 31, 43, 57, 58, and 59 along with the calculated percent that acetaldehyde, ethanol, allyl alcohol, propionaldehyde, and n-propanol are contributing to each signal.

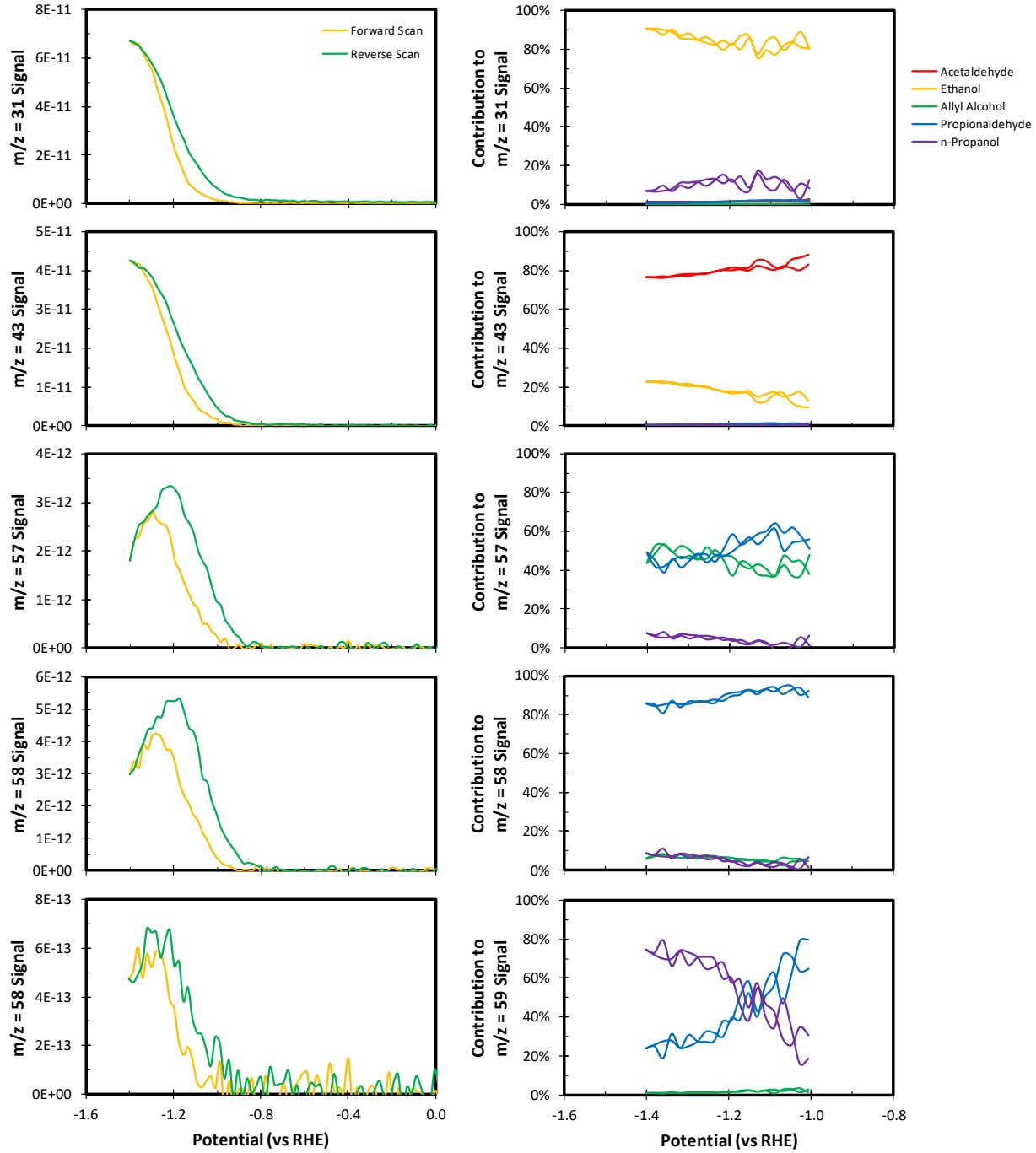

Figure S23 – Deconvolution of the m/z = 31, 43, 57, 58, and 59 mass-ion current signals observed over Cu during cyclic voltammetry at a scan rate of 1 mV/s in 0.1 M $CsHCO_3$ at a flow rate of 85 mL/min.

SI-16: Transient Ethene Generation Rate Before and After Cathodic Polarization

The transient activity of Cu for producing ethene (*m/z* = 26) was monitored at -1 V vs RHE before and after a brief cathodic polarization at -1.4 V vs RHE. As shown in Figure S24, the ethene partial current density was elevated after the brief cathodic polarization took ~5 min to decay back to the initial value. This suggests that the prior history of Cu can influence its transient activity for several minutes until steady state activity is reached.

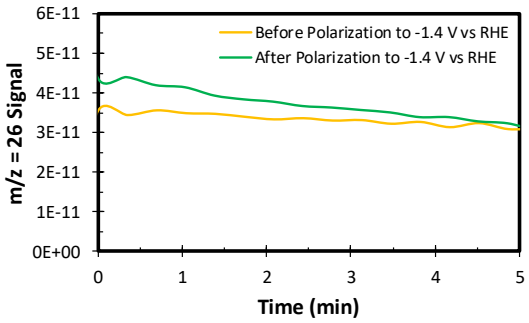

Figure S24 – Transient ethene (m/z = 26) generation rate over Cu at an applied potential of -1 V vs RHE before and after a brief cathodic polarization to -1.4 V vs RHE in 0.1 M $CsHCO_3$ at a flow rate of 85 mL/min.

SI-17: Analysis of the Pervaporate Collected over Cu by Liquid Chromatography

The relative abundance of the multi-carbon liquid-phase products produced over Cu as measured in a traditional H-cell using HPLC, the DEMS cell using MS, and the condensed DEMS cell pervaporate using HPLC are shown in Table S3. This data was utilized to calculate the molar ratio of aldehydes to the corresponding alcohols observed in each case. As shown in Table S4, the pervaporate of the DEMS cell had a higher abundance of aldehydes relative to alcohols when quantified by mass spectrometry or when condensed and analyzed by liquid chromatography. The aldehyde to alcohol ratio of the DEMS cell pervaporate was lower when condensed and quantified by HPLC than when quantified by MS, presumably due to the loss of aldehydes by evaporation when collecting the condensed pervaporate. This hypothesis is corroborated by the greater discrepancy of the aldehyde to alcohol ratio of the DEMS cell pervaporate as quantified by MS and HPLC for the C_2 products than the C_3 products, which occurs due to the higher volatility of acetaldehyde than propionaldehyde.

Table S3 – Relative abundance of the liquid-phase products produced over Cu as measured in a traditional H-cell via HPLC, the DEMS cell pervaporate by MS, and the condensed DEMS cell pervaporate by HPLC.

	H-Cell	DEMS	Condensed Pervaporate
Acetaldehyde	4.04%	61.85%	37.02%
Ethanol	71.75%	28.04%	59.65%
Allyl Alcohol	5.97%	1.72%	0.06%
Propionaldehyde	2.74%	5.86%	1.63%
n-Propanol	15.50%	2.53%	1.64%

Table S4 – Abundance of aldehydes relative to the corresponding alcohols observed over Cu as measured in a traditional H-cell via HPLC, the DEMS cell pervaporate by MS, and the condensed DEMS cell pervaporate by HPLC.

	H-Cell	DEMS	Condensed Pervaporate
Acetaldehyde/Ethanol	0.056	2.200	0.621
Propionaldehyde/n-Propanol	0.177	2.300	0.993